

Supporting Information for

Spatial Separation of Enantiomers by Field-Modulated Surface Scattering

Yun Chen,¹ Long Xu,² Michael Urbakh,¹ Oded Hod^{1*}

- 1 School of Chemistry and The Sackler Center for Computational Molecular and Materials Science, Tel Aviv University, Tel Aviv 6997801, Israel
- 2 AMOS and Department of Chemical and Biological Physics, The Weizmann Institute of Science, Rehovot 7610001, Israel

This supporting information document includes the following sections:

Section 1. Methods.....	2
1.1 Derivation of the light-molecule interaction terms	2
1.2 Molecule surface interaction term	6
1.3 Transformation validation tests	9
1.4 Energy conservation tests	11
Section 2. Separation of HSOH enantiomers.....	13
2.1 Rotational dynamics of HSOH ensemble of $N = 1,440$	13
2.2 Effect of friction coefficient on molecular scattering	15
2.3 Effect of static electric field strength on molecular orientation	16
2.4 Effect of incident velocity on molecular orientation	18
2.5 Quantum mechanical effects on molecular pre-orientation	20
2.6 Effect of molecular deformation on enantio-separation of HSOH	21
2.7 Thermal effects on HSOH enantio-separation	26
2.8 HSOH enantio-separation under parallel alignment conditions	28
2.9 HSOH enantiomeric scattering under a permanent uniform electric field	31
Section 3. Separation of propylene oxide (C₃H₆O) enantiomers.....	32
References	35

Section 1. Methods

1.1 Derivation of the light-molecule interaction terms

The field-induced torque experienced by the molecule at each time step of our simulation includes contributions due to the permanent molecular dipole moment, \mathbf{P}_0 , and the molecular polarizability tensor $\hat{\alpha}$. Considering first the effect of a static homogeneous external electric field, \mathbf{E}_{static} , the torque can be written as:

$$\boldsymbol{\tau}_{static} = (\mathbf{P}_0 + \mathbf{P}_{ind}) \times \mathbf{E}_{static} \quad (\text{S1})$$

where $\mathbf{P}_{ind} = \hat{\alpha}\mathbf{E}_{static}$ is the polarizability induced dipole moment. The corresponding energy contribution arises from the following term in the classical Hamiltonian of the system:

$$H_{static}(t) = -\sum_{i=x,y,z} P_{0,i} E_{static,i} - \frac{1}{2} \sum_{i,j=x,y,z} \alpha_{ij} E_{static,i} E_{static,j}. \quad (\text{S2})$$

Next, we consider the response of the system to time-dependent laser electric pulses of the form:

$$\mathbf{E}(t) = \boldsymbol{\varepsilon}(t) \cos(\omega t), \quad (\text{S3})$$

where ω is the pulse frequency,

$$\boldsymbol{\varepsilon}(t) = \mathbf{E}_0 \exp\left[-2 \ln(2) \frac{(t-t_0)^2}{\sigma^2}\right] \quad (\text{S4})$$

is the Gaussian envelope of the pulse, σ is the full width at half-maximum of the envelope, t_0 is the pulse center, and $|\mathbf{E}_0|$ is the pulse peak amplitude. Since in our simulations the pulse time-period ($2\pi/\omega$) is considerably shorter than the typical response time of the permanent molecular dipole moment, we neglect this contribution and consider only the induced dipole moment contribution due to the pulse envelope:

$$\boldsymbol{\tau}_{pulse} \approx \langle \hat{\mathbf{P}}_{ind}(t) \times \mathbf{E}(t) \rangle = \hat{\alpha} \langle \mathbf{E}(t) \times \mathbf{E}(t) \rangle = \frac{1}{2} \hat{\alpha} \boldsymbol{\varepsilon}(t) \times \boldsymbol{\varepsilon}(t), \quad (\text{S5})$$

where $\langle \cdot \rangle$ signifies a time-average over the optical cycle., which is due to the fact that the carrier frequency ω is larger than the typical rotation frequency of the molecule by several orders of magnitude, so that we can average over the rapid oscillations of the laser field in the simulations.¹⁻³ The corresponding Hamiltonian interaction energy term is given by:

$$H_{pulse}(t) = -\frac{1}{2} \langle \mathbf{E}^T(t) \hat{\alpha} \mathbf{E}(t) \rangle = -\frac{1}{4} \sum_{i,j=x,y,z} \varepsilon_i(t) \alpha_{ij} \varepsilon_j(t) \quad (\text{S6})$$

In our simulations, the permanent molecular dipole moment, \mathbf{P}_0 , and the polarizability tensor, $\hat{\alpha}$, are obtained via density functional theory calculations (DFT), using the Gaussian suite of programs.⁴ Following geometry optimization, the molecular coordinates are obtained such that the principal axes of the nuclear charges $\mathbf{C}_x, \mathbf{C}_y, \mathbf{C}_z$, which are the eigenvectors of the following tensor:

$$\hat{I}^C = \begin{pmatrix} \sum_n q_n (y_n^2 + z_n^2) & -\sum_n q_n x_n y_n & -\sum_n q_n x_n z_n \\ -\sum_n q_n y_n x_n & \sum_n q_n (x_n^2 + z_n^2) & -\sum_n q_n y_n z_n \\ -\sum_n q_n z_n x_n & -\sum_n q_n z_n y_n & \sum_n q_n (x_n^2 + y_n^2) \end{pmatrix}, \quad (\text{S7})$$

are along the (1,0,0), (0,1,0), and (0,0,1) directions, respectively. Here, q_n is the nuclear charge of atom n , $\mathbf{R}_n = (x_n, y_n, z_n)$ are the coordinates of atom n in the optimized molecule given in some general orientation, and the sum runs over all atoms in the molecule. We note that the eigenvectors $\mathbf{C}_x, \mathbf{C}_y, \mathbf{C}_z$ are ordered such that the corresponding eigenvalues fulfill the following relation: $c_x \leq c_y \leq c_z$. Correspondingly, the permanent dipole moment and polarizability tensor are given in the same reference frame and are marked as \mathbf{P}_0^C and $\hat{\alpha}^C$. We also mark as (x_n^C, y_n^C, z_n^C) the coordinates of atom n in the C reference frame.

Next, the optimized molecule is rigidly shifted such that its center of mass (rather than the center of nuclear charge) is at the origin, obtaining new molecular coordinates $\tilde{\mathbf{R}}_n^C = (\tilde{x}_n^C, \tilde{y}_n^C, \tilde{z}_n^C)$. Then, the molecule is rotated to align its principal inertia axes $\mathbf{M}_x, \mathbf{M}_y, \mathbf{M}_z$, which are the eigenvectors of the molecular inertia tensor:

$$\hat{I}^M = \begin{pmatrix} \sum_n m_n (\tilde{y}_n^{C^2} + \tilde{z}_n^{C^2}) & -\sum_n m_n \tilde{x}_n^C \tilde{y}_n^C & -\sum_n m_n \tilde{x}_n^C \tilde{z}_n^C \\ -\sum_n m_n \tilde{y}_n^C \tilde{x}_n^C & \sum_n m_n (\tilde{x}_n^{C^2} + \tilde{z}_n^{C^2}) & -\sum_n m_n \tilde{y}_n^C \tilde{z}_n^C \\ -\sum_n m_n \tilde{z}_n^C \tilde{x}_n^C & -\sum_n m_n \tilde{z}_n^C \tilde{y}_n^C & \sum_n m_n (\tilde{x}_n^{C^2} + \tilde{y}_n^{C^2}) \end{pmatrix}, \quad (\text{S8})$$

with the axes of the laboratory frame, defined as (1,0,0), (0,1,0), and (0,0,1), respectively. In Eq. S8 m_n denotes the mass of atom n . Here, as well, the eigenvectors $\mathbf{M}_x, \mathbf{M}_y, \mathbf{M}_z$ are ordered such that the corresponding eigenvalues fulfill the relation: $m_x \leq m_y \leq m_z$. The transformation is performed as follows:

$$\mathbf{R}_n^M = \hat{C}^{MC} \tilde{\mathbf{R}}_n^C, \quad (\text{S9})$$

where \hat{C}^{MC} is the direction cosine matrix, whose elements, \hat{C}_{ij}^{MC} , are the cosines of the angles between the M_i and C_j axes. Correspondingly, \mathbf{P}_0^C and $\hat{\alpha}^C$ are transformed to the same reference frame as follows:

$$\begin{cases} \mathbf{P}_0^M = \hat{\mathbf{C}}^{MC} \mathbf{P}_0^C \\ \hat{\boldsymbol{\alpha}}^M = \hat{\mathbf{C}}^{MC} \hat{\boldsymbol{\alpha}}^C (\hat{\mathbf{C}}^{MC})^T, \end{cases} \quad (\text{S10})$$

allowing for the calculation of the total torque acting on the molecule using Eqs. S1 and S5.

Given the total molecular torque, $\boldsymbol{\tau} = \boldsymbol{\tau}_{static} + \boldsymbol{\tau}_{pulse}$, in the M reference frame, the forces acting on each atom due to the action of the static electric field and the electric pulse can then be deduced from the following relation:

$$\boldsymbol{\tau} = (I_x^M \dot{\omega}_x^M, I_y^M \dot{\omega}_y^M, I_z^M \dot{\omega}_z^M), \quad (\text{S11})$$

where \mathbf{I}^M is the molecular inertial moment vector, formed from the eigenvalues of the matrix \hat{I}^M , and $\dot{\boldsymbol{\omega}}^M$ is the molecular angular acceleration vector. The angular accelerations calculated via Eq. (S11) are then used to obtain the force acting on the individual atoms in the molecule as follows:

$$\mathbf{F}_n^M = m_n (\dot{\omega}_x^M d_x, \dot{\omega}_y^M d_y, \dot{\omega}_z^M d_z), \quad (\text{S12})$$

where d_i is the minimal distance between the atom and inertial axis I_i^M .

The above procedure, provides the forces acting on the various atoms of a molecule, whose inertia axes are aligned with the Cartesian axes, due to a static electric field and a laser pulse acting in arbitrary directions. Naturally, in our simulations, the inertia axes of the molecule are not necessarily aligned with the Cartesian axes. Hence, to obtain the force acting on a molecule in an arbitrary orientation in space, we first transform the molecule and the corresponding fields to the M basis, then we evaluate the forces, and finally, we rotate the latter back to the original (arbitrary) orientation.

We first consider rigid molecules (of the geometry optimized structure) in some random orientation in space, whose atomic coordinates are $\{\mathbf{R}_n^R\}$ in the laboratory frame. The inertia axes of the molecule are calculated according to Eq. S8, with $\{\tilde{\mathbf{R}}_n^C\}$ replaced by $\{\mathbf{R}_n^R\}$. Next, the direction cosine matrix, $\hat{\mathbf{C}}^{MR}$, whose elements $\hat{\mathbf{C}}_{ij}^{MR}$ are the cosine angles between the inertia axes $i = \mathbf{M}_x^R, \mathbf{M}_y^R, \mathbf{M}_z^R$, and the directional unit vectors $j = (1,0,0), (0,1,0),$ and $(0,0,1)$, is calculated. As mentioned above, \mathbf{M}_x^R and \mathbf{M}_z^R are associated with the smallest and largest eigenvalues, respectively. This matrix is used to transform the static electric field, \mathbf{E}_{static}^R , and pulse, $\boldsymbol{\varepsilon}^R(t)$, vectors to the M reference frame as follows:

$$\begin{cases} \mathbf{E}_{static}^M = \hat{\mathbf{C}}^{MR} \mathbf{E}_{static}^R \\ \boldsymbol{\varepsilon}^M(t) = \hat{\mathbf{C}}^{MR} \boldsymbol{\varepsilon}^R(t) \end{cases} \quad (\text{S13})$$

This allows us to calculate the forces acting on each atom in the M reference frame, \mathbf{F}_n^M (Eq. S12), according to the procedure defined above (Eqs. S1-S12), based on the DFT calculated permanent dipole moment and polarizability tensor.

Finally, the forces are transformed back to match the instantaneous random orientation of the molecule as follows:

$$\mathbf{F}_n^R = \widehat{\mathbf{C}}^{MR^T} \mathbf{F}_n^M, \quad (\text{S14})$$

allowing for performing the molecular dynamics step.

For simulations involving flexible molecules, we adopt the same procedure discussed above, while assuming that the molecular distortions are sufficiently small to induce negligible variations in the permanent dipole moment, the polarizability tensor, and the inertia vectors with respect to those of the reference relaxed molecule. This assumption is verified in section 1.3 below.

1.2 Molecule surface interaction term

To describe the interactions between atom i of the scattering molecule and the semi-infinite homogeneous scattering surface assumed to consist of atoms of type j only, we adopt the following Lennard-Jones (LJ) 9-3 potential expression:⁵

$$V_{ij}(r_{\perp}) = \epsilon_{9-3}^{ij} \left[\frac{2}{15} \left(\frac{\eta_{9-3}^{ij}}{r_{\perp}} \right)^9 - \left(\frac{\eta_{9-3}^{ij}}{r_{\perp}} \right)^3 \right], \quad (\text{S15})$$

where r_{\perp} is the vertical distance between the atom and the wall, and ϵ_{9-3}^{ij} and η_{9-3}^{ij} are parameters that determine the energy and length scale of the particle-wall interaction, respectively. This potential is obtained by integrating the pairwise LJ 12-6 potential over the semi-infinite substrate. The relations between the LJ 9-3 and LJ 12-6 parameters are given by:

$$\eta_{9-3}^{ij} = \eta_{12-6}^{ij} \quad ; \quad \epsilon_{9-3}^{ij} = \frac{2\pi\rho_{\text{substrate}}}{3} (\eta_{12-6}^{ij})^3 \epsilon_{12-6}^{ij} \quad (\text{S16})$$

where $\rho_{\text{substrate}}$ corresponds to the atomic density of the substrate.

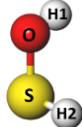
The parameters for the molecule-surface interaction potential are obtained using the Lorentz-Berthelot combination rules, according to which the heterogeneous parameters are obtained from their homogeneous counterparts, as follows:

$$\eta_{12-6}^{ij} = \frac{\eta_{12-6}^{ii} + \eta_{12-6}^{jj}}{2} \quad (\text{S17})$$

$$\epsilon_{12-6}^{ij} = \sqrt{\epsilon_{12-6}^{ii} \epsilon_{12-6}^{jj}}. \quad (\text{S18})$$

Table S1 gives the homogeneous 12-6 interaction parameters taken from Ref. [6] for graphitic carbon atoms and from Ref. [7] for the atoms of the HSOH molecule as given in the OPLS-AA force field.

Table S1: Summary of LJ 12 – 6 homogeneous parameters for HSOH and graphene.

Molecule	Atom	η_{12-6}^{ii} (Å)	ϵ_{12-6}^{ii} (kcal/mol)
HSOH 	H	2.95	0.03
	O	3.165	0.28
	S	3.48	0.395
Graphene	C	3.4	0.06549

To assess the sensitivity of the enantio-separation results to the choice of LJ parameters, we repeated some of the flexible molecular scattering calculations while modifying ϵ_{9-3}^{iC} separately for each atom in the molecule and for all of them together in the range $\pm 30\%$ around the values obtained from Table S1 via Eq. S18. Fig. S1 presents the dependence of the enantiomeric excess as a function of ϵ_{9-3}^{iC} for $i = H$ (red circles), $i = O$ (blue triangles), $i = S$ (purple triangles), and for all of them together (black squares).

The largest relative variations in the calculated enantiomeric excess are within the range -18.91% and $+4.72\%$ for the entire range of ϵ_{9-3}^{HC} values considered. Naturally, the highest sensitivity is obtained for the parameters of the H atom, which is the closest to the scattering surface. Notably, for the entire LJ parameter range considered, a significant enantio-separation excess is achieved, indicating that the qualitative nature of our results is robust against variations in the simulation parameters.

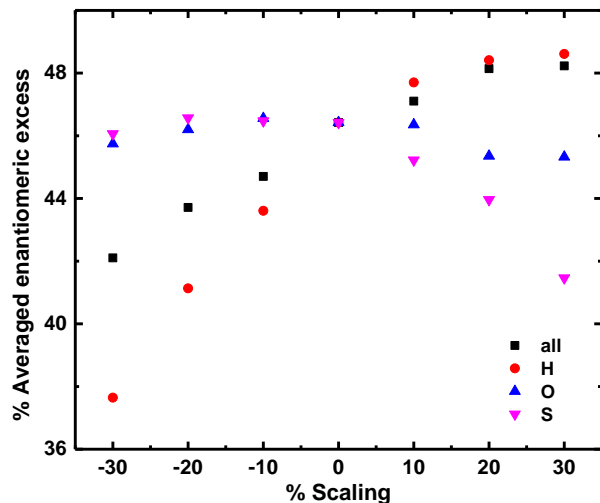


Figure S1: Sensitivity test of the enantio-separation excess as a function of relative variation of the ϵ_{9-3}^{iC} LJ parameter for $i = H$ (red circles), $i = O$ (blue triangles), $i = S$ (purple triangles), and for all of them together (black squares). The simulations are performed for an ensemble of 18,000 randomly oriented flexible HSOH molecules given an initial center-of-mass velocity of 300 m/s towards a frictional wall with a kinetic friction coefficient of $\mu_k = 0.3$. The molecules are subjected to a Gaussian electric pulse ($\sigma = 0.1$ ps, $E_0 = 84.85$ MV/cm, and $t_0 = 0.5$ ps, see main text) at the beginning of the simulation and to a static field of 500 kV/cm, switched on parallel to the wall with a delay of 2.25 ps from the pulse peak intensity and switched off after 0.7 ps.

1.3 Transformation validation tests

In this study, all molecular geometries and dielectric parameters were obtained via DFT calculations performed at the CAM-B3LYP/aug-cc-pVTZ level of theory using the Gaussian 16 package.⁸ All dielectric parameters were obtained for the optimized molecular coordinates. Table S2 presents the relevant properties of one of the HSOH enantiomers (e_2) in the C and M reference frames (see section 1.1 above), including eigenvalues of the inertia tensor, permanent dipole moment, and independent polarizability tensor elements.

Table S2: Eigenvalues of the inertia tensor, components of the permanent dipole moment, and independent polarizability tensor elements calculated for one of the HSOH enantiomers. All values are presented in both the C and M reference frames. For the complementary enantiomer, the values of $P_{0,x}$, α_{xy} and α_{xz} have opposite signs.

Molecule	In the C reference frame				In the M reference frame			
	Moments of inertia (a. u.)	Dipole moment components (Debye)	Polarizability tensor components (a. u.)		Moments of inertia (a. u.)	Dipole moment components (Debye)	Polarizability tensor components (a. u.)	
HSOH (e_2)	$I_x = 8.4$	$P_{0,x} = 0.042$	$\alpha_{xx} = 32.158$	$\alpha_{xy} = -1.014$	$I_x = 16,099$	$P_{0,x} = -0.018$	$\alpha_{xx} = 32.044$	$\alpha_{xy} = 1.207$
	$I_y = 65.3$	$P_{0,y} = 0.788$	$\alpha_{yy} = 26.641$	$\alpha_{xz} = 0.488$	$I_y = 215,680$	$P_{0,y} = 0.758$	$\alpha_{yy} = 26.715$	$\alpha_{xz} = 0.653$
	$I_z = 68.6$	$P_{0,z} = 1.420$	$\alpha_{zz} = 26.742$	$\alpha_{yz} = 0.031$	$I_z = 221,805$	$P_{0,z} = -1.437$	$\alpha_{zz} = 26.782$	$\alpha_{yz} = 0.029$

These parameters, were used for describing the molecular interaction with the static electric field and the laser pulse (see section 1.1 above) within the LAMMPS package⁹.

To check the validity of our implementation, we chose 1,500 uniformly distributed random molecular orientations of the optimized HSOH geometry and calculated their permanent dipole moment and polarizability tensors via DFT calculations. Comparing the results to those obtained by rotation of the dipole moment and polarizability tensor calculated once at the reference molecular orientation (see section 1.1 above), we find ensemble root mean square deviations that do not exceed 2.5% (see Table S3). These residual deviations result from the fact that at some orientations the absolute values calculated are comparable to the numerical accuracy of the rotation procedure and the DFT calculations. Altogether, this analysis verifies the validity of our procedure for evaluating the molecular dipole moment and polarizability tensor.

Next, to verify the validity of our assumption that molecular flexibility has minor effect on the values of the permanent dipole moment and polarizability tensor elements, we performed 1,500 zero temperature MD simulations without surface scattering, starting from 1,500 uniformly distributed random

orientations of the geometry optimized molecules and applying a static electric field of 5,000 kV/cm. During these simulations, the molecules were allowed to rotate and vibrate freely, while their center of mass remained fixed, due to molecular neutrality. For each simulation, we took a molecular snapshot after 200 ps and calculated the dipole moment and polarizability tensor using DFT. Comparing the results to those obtained for the optimized molecule (see section 1.1 above), we find that the ensemble root mean square deviations do not exceed 8% (see Table S3). Given the 2.5% deviation obtained for the rigidly rotated geometry optimized molecules, we conclude that the effect of molecular flexibility is less than 5.5%. These findings are in line with the results presented in Fig. S11 below, where prior to the collision, the flexible molecules exhibit minor deformation due to the interaction with the external fields.

Table S3: Validity test of the algorithm for evaluating the permanent dipole moment and polarizability tensor of randomly oriented optimized and flexible HSOH molecules. The values reported represent the ensemble root mean square relative deviations between DFT results obtained at the random molecular orientations and at the reference frame by appropriate rotation.

Molecule	Ensemble root mean square deviations with respect to the optimized molecule in the reference frame (%)								
	$P_{0,x}$	$P_{0,y}$	$P_{0,z}$	α_{xx}	α_{yx}	α_{yy}	α_{zx}	α_{zy}	α_{zz}
Optimized rigid HSOH molecules	0.556	0.037	0.019	0.002	2.073	0.002	1.528	1.293	0.002
Flexible HSOH molecules	4.457	2.408	1.759	0.026	6.958	0.031	2.235	7.672	0.025

1.4 Energy conservation tests

To verify energy conservation during the dynamics, we performed a set of simulations of HSOH molecular ensembles initially prepared at uniformly distributed random spatial orientations. First, we evaluated energy conservation in the absence of a scattering wall. To this end, we constructed a molecular ensemble consisting of 1,500 rigid molecules and subjected it to uniform static electric fields of 50, 500, and 5,000 kV/cm. Panels a-c of Fig. S2 present the energy as a function of time for the three fields, respectively. In each panel, three fixed propagation time steps are considered, 0.01 (red), 0.05 (blue), and 0.1 (yellow) fs. In all cases, energy is found to conserve, where conservation improves with decreasing time-step (lower fluctuations).

When considering flexible molecules, high-frequency bond oscillations develop making energy conservation more challenging to maintain with feasible fixed time-step values. For the lower field considered (Fig. S2d) the average energy seems to be stable, but the fluctuations are orders of magnitude higher than those obtained for the rigid case (Fig. S2a) even at the smallest time-step considered. For the higher field values evaluated (Fig. S2e, f), energy conservation is very poor with the time-steps considered. We note however, that in the present study we apply the static field for a duration no longer than 1 ps, after which the molecule propagates freely towards the wall. Therefore, the propagation error under the field does not build up and energy conservation is satisfied even for the time-steps used herein, as demonstrated in Fig. S3b below. Furthermore, since we already established that the effect of molecular flexibility is relatively small in our case, all simulations presented in the main text were performed with rigid molecules, where energy conservation is well satisfied with our choice of parameters.

Next, we evaluated energy conservation in the presence of a scattering wall. To this end, we constructed an ensemble of 3,000 randomly oriented flexible molecules and subjected them to the full manipulation protocol, including an alignment pulse followed by an orienting static electric field (the corresponding simulation parameters appear in the caption of Fig. S3). Fig S3a presents the total energy (red) and its kinetic (blue) and potential (yellow) energy components as functions of time for frictionless scattering. The total energy spike appearing at 0.5 ps corresponds to the application of the external pulse. Similar, yet smaller in magnitude, total energy variations occur at 2.75 and 3.45 ps (see Fig S3b) corresponding to the switching on and off of the static electric field, respectively. In the absence of external fields, the total energy conserves well (on the noted scale) during the entire scattering process up to 10 ps simulation time, even when the kinetic and potential energy terms exchange energy upon collision. When

surface friction is included in the simulation, the molecule loses kinetic energy during the collision, resulting in total energy reduction, as long as the molecule is within the frictional interaction range (see Fig. S3c).

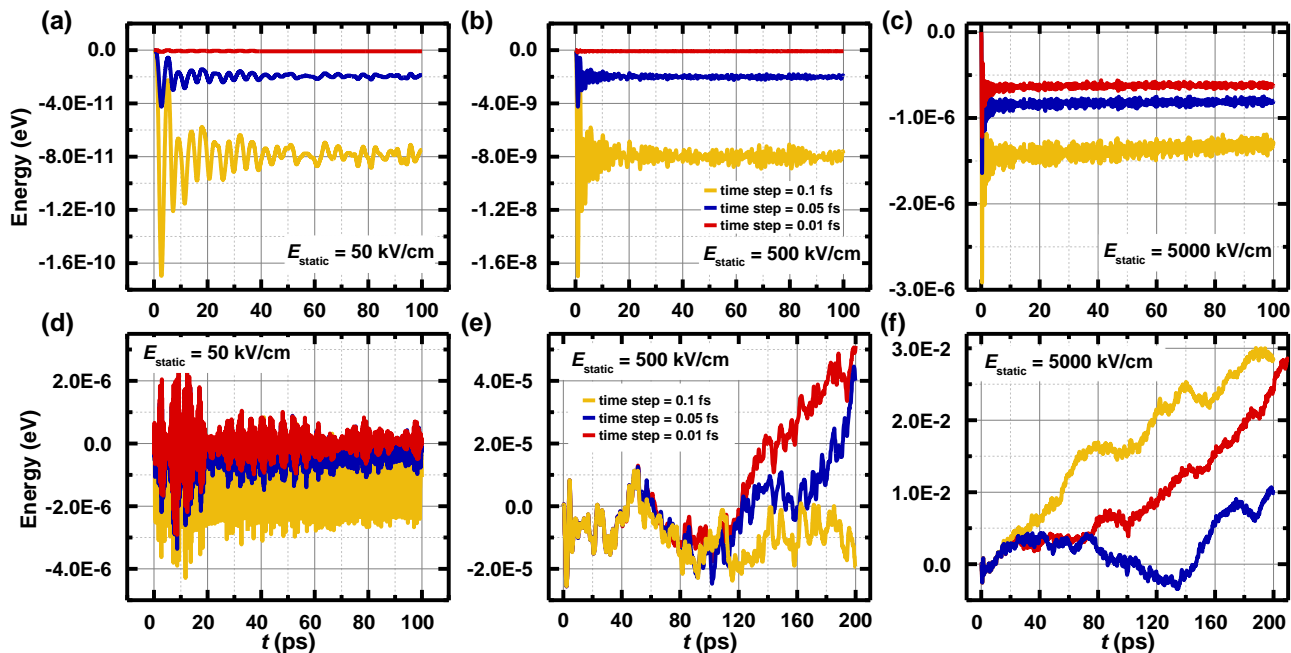


Figure S2: Energy conservation tests for an ensemble of 1,500 rigid (panels a-c) and flexible (panels d-f) HSOH molecules interacting with static uniform electric fields of 50 (a, d), 500 (b, e), and 5,000 (c, f) kV/cm. In each simulation, three time-steps are considered: 0.01, 0.05, and 0.1 fs, marked in red, blue, and yellow, respectively.

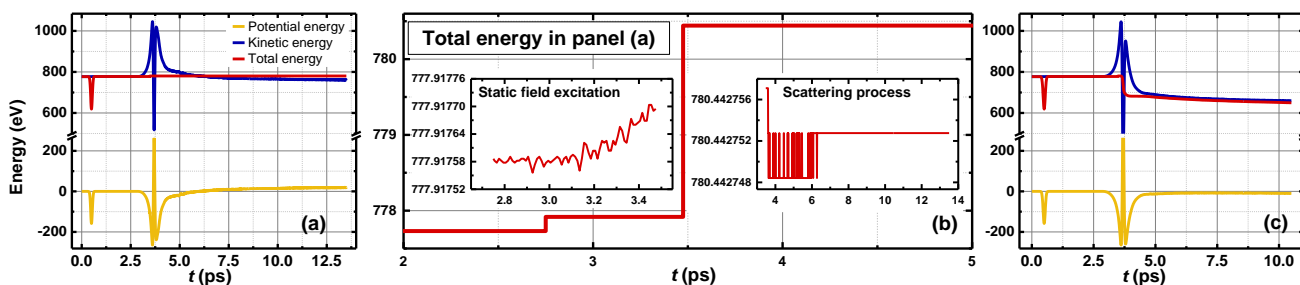


Figure S3: Energy conservation tests for an ensemble of 3,000 randomly oriented flexible HSOH molecules initially positioned 4 nm above a frictionless (panels (a) and (b)) or a frictional (friction coefficient of $\mu_k = 0.3$, panel (c)) wall and given an initial normal center-of-mass velocity of 1,000 m/s. The molecules are subjected to a Gaussian electric pulse ($\sigma = 0.1$ ps, $E_0 = 84.85$ MV/cm, and $t_0 = 0.5$ ps, see main text) at the beginning of the simulation and to a static field of 500 kV/cm, switched on parallel to the wall with a delay of 2.25 ps from the pulse peak intensity and switched off after 0.7 ps. Panel (b) provides a zoom-in on the total energy curve appearing in panel (a) for the frictionless scattering case, where the insets give a further zoom-in on the regions where the static field is applied and when surface scattering occurs.

Section 2. Separation of HSOH enantiomers

2.1 Rotational dynamics of HSOH ensemble of $N = 1,440$

In Fig. 2b of the main text, we presented anharmonic ensemble averaged rotational dynamics of an ensemble of 1,440 HSOH molecules. In this ensemble, the initial orientation of the SO bond of all molecules was placed along the vertical axis, while the azimuthal angle of the permanent molecular dipole moment with respect to the field direction was uniformly distributed. The anharmonic behavior was attributed to this uniform distribution, which includes large azimuthal angles, beyond the linear regime.

To demonstrate this, we present in Fig. S4 the azimuthal angle dynamics for the entire ensemble of molecules (thin colored lines) and their average (thick red line) under the effect of a uniform constant electric field of $E = 50$ kV/cm in the positive Y direction. At the beginning of the dynamics, all molecular dipoles rotate toward the direction of the electric field. This synchronized motion results in the initial increase of the ensemble averaged cosine angle $\langle \cos(\chi) \rangle$. Nevertheless, different initial azimuthal angles yield trajectories of different periods, where for small initial angles (with respect to the field direction) the behavior is harmonic, whereas for large initial angles it turns anharmonic. This resembles the case of a classical pendulum, where the oscillation period is independent of the initial angle only for small oscillation amplitudes. As a result, after reaching the initial ensemble averaged peak, dipole synchronization is lost, and the ensemble averaged cosine angle reduces towards a lower stable value, carrying residual periodic oscillations that decay with time.

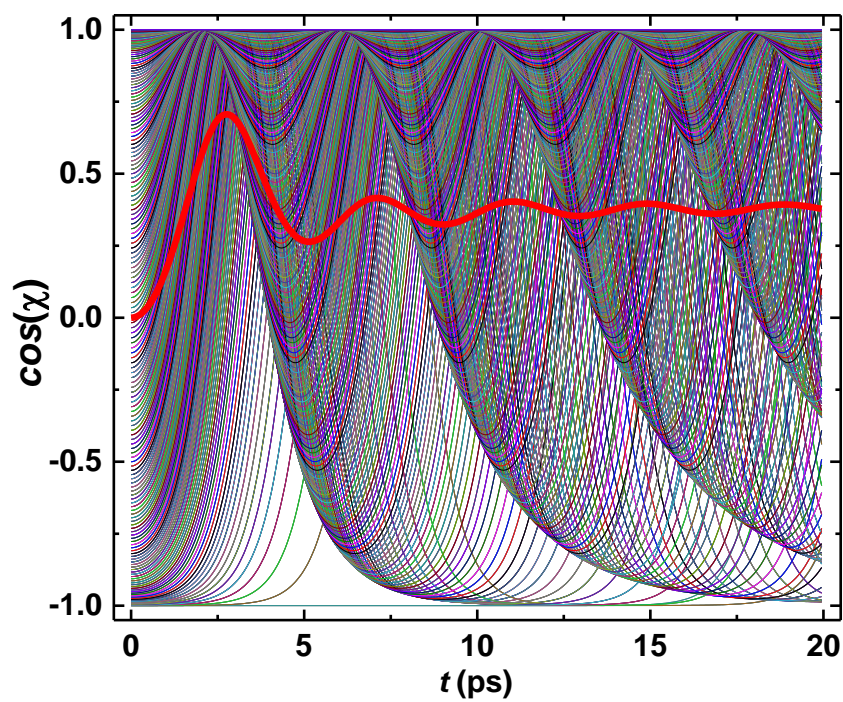


Figure S4: Azimuthal angle dynamics ($\cos(\chi)$) for an ensemble of 1,440 HSOH pre-aligned rigid molecules (thin colored lines) and their average ($\langle \cos(\chi) \rangle$), thick red line) under the effect of a uniform constant electric field of $E = 50 \text{ kV/cm}$ in the positive Y direction.

2.2 Effect of friction coefficient on molecular scattering

In Fig. 2c of the main text, we showed that the enantiomeric excess is practically independent of the surface kinetic friction coefficient. To rationalize this result, we examined the molecular scattering trajectories of the perfectly oriented enantiomers under various friction coefficients. As shown in Fig. S5, the value of the kinetic friction coefficient has a minor effect on the azimuthal molecular scattering angle over many decades ($\mu_k = 10^{-8}$ to 0.01). This is the reason for the mild effect we find for the friction coefficient on the spatial enantio-separation efficiency. Nonetheless, friction is found to significantly affect the altitude scattering angle (the angle between the center of mass velocity vector of the scattered molecule and the vertical axis), indicating that the two enantiomer collection regions do depend on the value of the friction coefficient in this range. At higher friction coefficients, a significant impact is observed for both the azimuthal and altitude angles.

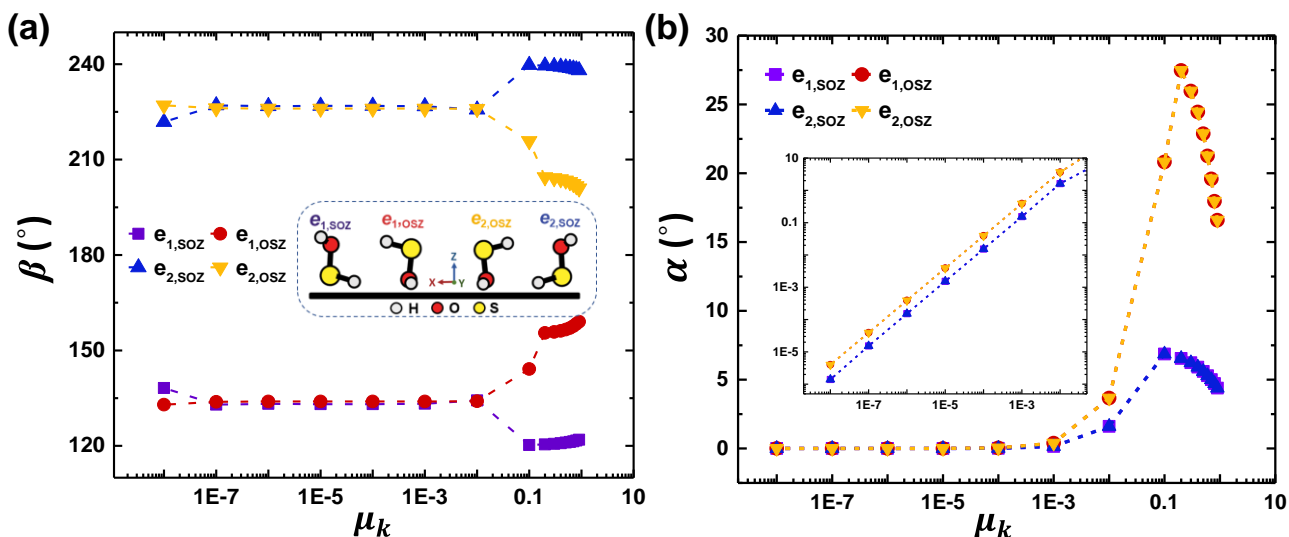


Figure S5: Dependence of the (a) azimuthal (measured with respect to the Y-axis) and (b) altitude (measured with respect to the Z-axis) angles of surface scattered HSOH enantiomers on the friction coefficient. The pre-oriented molecules (see inset of panel (a)) are released at an initial height of 2 nm above the surface with a normal center of mass velocity of 1000 m/s. The simulation runs for 8 ps.

2.3 Effect of static electric field strength on molecular orientation

In Fig. 4a of the main text, a non-monotonic dependence of the enantio-separation efficiency on the strength of the static uniform field was demonstrated. It was argued that at low field strengths the ensemble does not achieve optimal average orientation prior to the impact with the scattering wall, whereas at high field strengths the molecular ensemble accumulates high angular momentum and hence loses orientation during collision. As a result, maximal enantio-separation efficiency is achieved at intermediate field strengths.

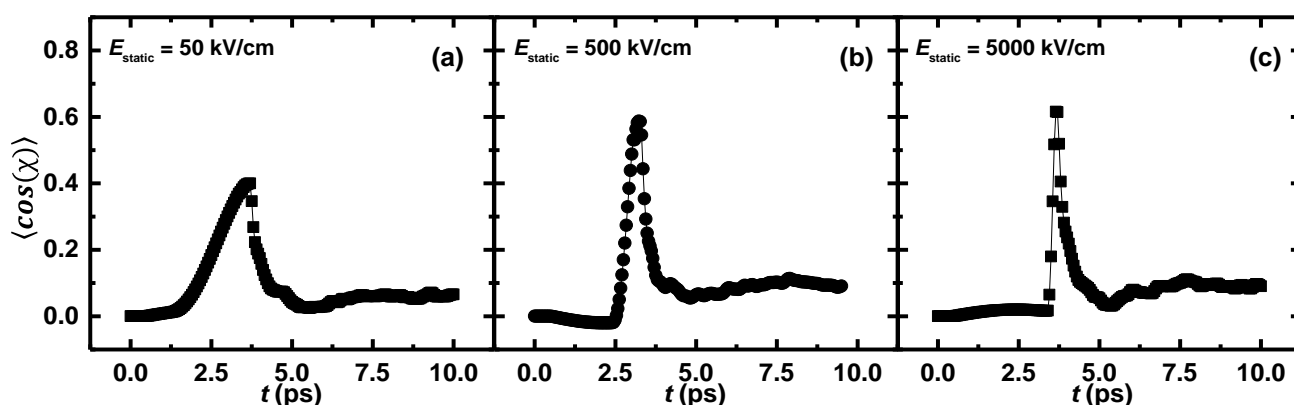


Figure S6: Time dependence of the ensemble averaged orientation factor $\langle \cos(\chi) \rangle$ under static field strengths of (a) 50, (b) 500, and (c) 5,000 kV/cm, corresponding to Fig. 4a of the main text. The center-of-mass of each molecule is placed 40 Å above a surface of kinetic friction coefficient $\mu_k = 0.3$ and given an initial vertical center-of-mass velocity of 1,000 m/s. A Gaussian electric pulse ($\sigma = 0.1$ ps, $E_0 = 84.85 \frac{\text{MV}}{\text{cm}}$, and $t_0 = 0.5$ ps) is applied at the beginning of the simulation and the static fields are switched on along the Y-direction with delays of 0.8, 2.25, and 2.9 ps, respectively, from the maximal pulse intensity, yielding the maximal enantio-separation efficiency in each case. Collision occurs at ~ 3.7 ps.

To support this statement, we present in Fig. S6 the time evolution of the ensemble averaged orientation factor ($\langle \cos(\chi) \rangle$) under the static field strengths of 50, 500, and 5,000 kV/cm considered in Fig. 4(a) of the main text. The overall orientation factor dynamics is similar in all case, where an initial rise, due to the application of the field, is followed by an abrupt reduction upon turning-off the field and surface collision, and stabilization around a small finite value. Important differences, however, are observed between the three cases. When increasing the field strength from 50 to 500 kV/cm, the initial rise becomes sharper and the peak value increases. This signifies a faster and more efficient orientation of the molecular ensemble, leading to an increase in the enantio-separation efficiency. Further increasing

the field to 5,000 kV/cm results in an even steeper initial increase of the orientation factor with little effect on its peak value. Notably, due to the higher angular momentum accumulated by the molecules in this case (see Fig. S7), the ensemble orientation is rapidly lost already during the collision period, as manifested by the sharp decrease in the orientation factor in Fig. S6c. This, in turn, harms the overall efficiency of the frictional enantio-separation process.

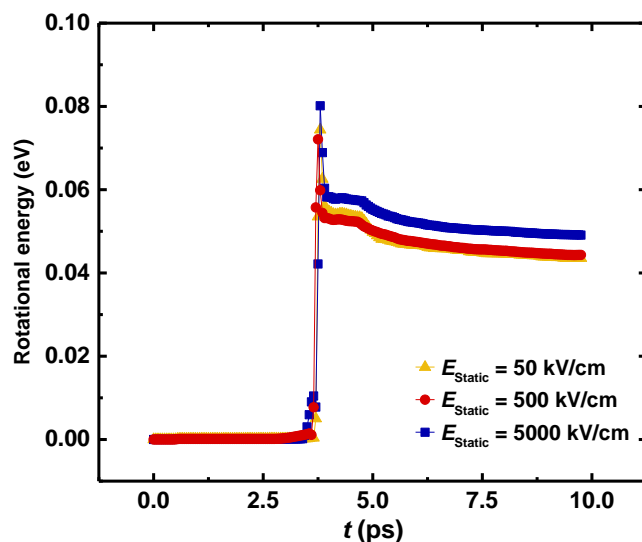


Figure S7: Time-dependence of the ensemble averaged molecular rotational energy under static electric fields of 50 (yellow triangles), 500 (red circles) and 5,000 (blue squares) kV/cm. All other simulation parameters are the same as in Fig. S6. Collision occurs at ~ 3.7 ps.

2.4 Effect of incident velocity on molecular orientation

In Fig. 4b of the main text, a reduction of the enantio-separation efficiency with increasing incident velocity was presented. This was attributed to the transfer of center-of-mass kinetic energy to molecular rotational energy upon collision with the surface. It was argued that at higher incident velocities, the molecules accumulate higher angular momentum during collision, which results in faster deviation of the ensemble distribution from the optimal dipole orientation and reduced enantio-selectivity.

To demonstrate this, we present in Fig. S8 the ensemble averaged rotational energy as a function of time for three incident molecular center-of-mass velocities, showing that with increasing velocity, the scattering molecules accumulate higher rotational energy. Fig. S9 presents the corresponding molecular orientation factor $\langle \cos(\chi) \rangle$ dynamics, demonstrating that the accumulated rotational energy at higher incident velocities results in a steeper reduction of the ensemble averaged molecular orientation upon collision. This, in turn, reduces the enantio-separation efficiency.

The insets in Fig. S9 show the molecular center-of-mass vertical position as a function of time. Showing that at low incident velocities, the molecules do not carry sufficient kinetic energy to scatter back from the frictional wall and remain trapped at the surface (see Fig. S9a), thus eliminating spatial enantio-separation.

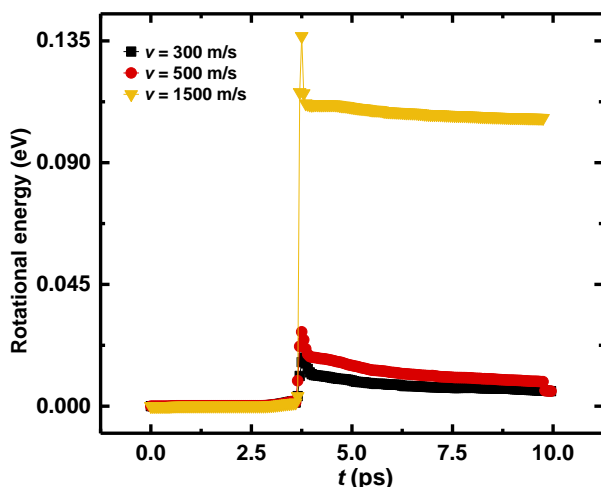


Figure S8: Time evolution of the ensemble averaged rotation energy for center-of-mass incident velocities of 300, 500, and 1,500 m/s. The initial heights above the surface are set to 15.8, 22.25, and 58.25 Å, respectively, such that collision occurs at ~ 3.7 ps. All other simulation parameters are the same as in Fig. S6b.

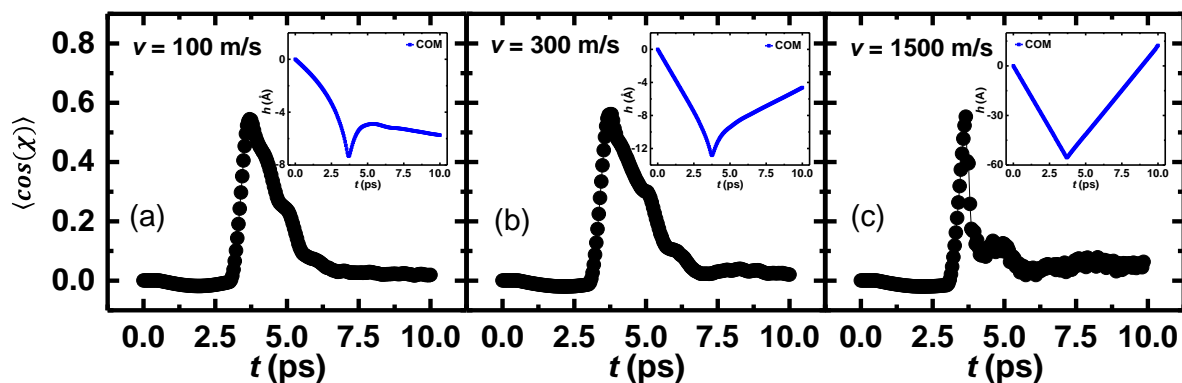


Figure S9: Time dependence of the ensemble averaged orientation factor $\langle \cos(\chi) \rangle$ for center-of-mass incident velocities of (a) 100, (b) 300, and (c) 1500 m/s, corresponding to Fig. 4b of the main text. All simulation parameters are the same as in Fig. S8. Collision occurs at ~ 3.7 ps.

Notably, contemporary technology allows to control the center of mass velocity spread of supersonic molecular beams down to 1%.¹⁰ As can be seen from the sensitivity test presented in Table S4, such narrow distributions reduce the impact of velocity spread on the enantioseparation down to $\sim 1\%$.

Table S4: Effect of velocity spread on enantiomeric excess under a static electric field strength of 500 kV/cm, corresponding to the black line in Fig. 4b in the main text. Relative deviations are shown in brackets.

Velocity (m/s)	Enantiomeric excess				
	99% velocity		101% velocity		100% velocity
300	47.84	(-0.60 %)	48.08	(-0.11 %)	48.13
500	43.93	(-1.03 %)	43.86	(-1.19 %)	44.39
1000	37.28	(-1.17 %)	37.45	(-0.72 %)	37.72
1500	31.62	(-1.31 %)	31.75	(-0.92 %)	32.04

2.5 Quantum mechanical effects on molecular pre-orientation

All calculations presented in the main text have been performed using classical mechanics simulations. To validate that quantum mechanical effects have minor influence on our simulation results and main conclusions, we performed test simulations considering quantum mechanical dynamics of the HSOH molecules under the effect of the classical alignment pulse and orientating static field. Technical details regarding the quantum-mechanical simulations, can be found in Refs. [11] and [12].

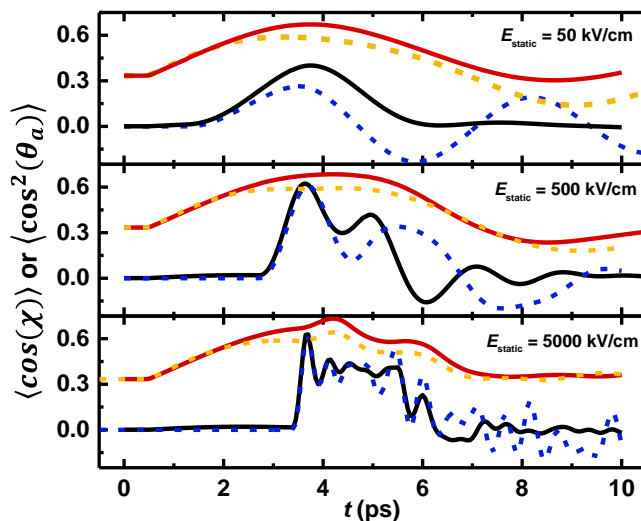


Figure S10: Comparison between classical (full red and black lines) and quantum mechanical (dashed yellow and blue lines) alignment (red and yellow lines) and orientation (black and blue lines) factor dynamics of an initially randomly oriented ensemble of $N = 18,000$ rigid HSOH molecules under static field strengths of 50 (upper panel), 500 (middle panel), and 5,000 (lower panel) kV/cm, applied at time delays of 0.8, 2.25, and 2.9 ps from the peak alignment pulse intensity, respectively. The alignment pulse parameters are as in Fig. S6.

Figure S10 compares the time evolution of the alignment and orientation factors $\langle \cos^2(\theta_a) \rangle$ and $\langle \cos(\chi) \rangle$ of an initially randomly oriented ensemble of $N = 18,000$ HSOH rigid molecules calculated via classical and quantum mechanical simulations. For the highest static field strength considered, the molecules acquire high angular momentum, such that the agreement between the quantum and classical mechanical results is excellent throughout the simulation period in line with the correspondence principle. For the smaller fields considered, some deviations between the two appear at $\sim 2 - 3$ ps following the peak of the alignment pulse. Notably, scattering occurs at ~ 3.7 ps, when the deviations of the classical ensemble averages from their quantum mechanical counterparts are still minor. This justifies our choice of classical dynamics simulations for the description of the pre-orientation process.

2.6 Effect of molecular deformation on enantio-separation of HSOH

The enantio-separation results presented in the main text were obtained via rigid molecule scattering simulations. To validate that molecular flexibility has minor influence on our simulation results and main conclusions, we performed test simulations considering the motion of the internal molecular degrees of freedom. To this end, we assume harmonic energy terms for all covalent bonds and angles, and the dihedral angle as follows:

$$E_{ij}^{bond} = \frac{1}{2} K_{ij}^{bond} (r_{ij} - r_{ij}^0)^2 \quad (\text{S19})$$

$$E_{ijk}^{angle} = \frac{1}{2} K_{ijk}^{angle} (\theta_{ijk} - \theta_{ijk}^0)^2 \quad (\text{S20})$$

$$E_{ijkl}^{dihedral} = \frac{1}{2} K_{ijkl}^{dihedral} (\phi_{ijkl} - \phi_{ijkl}^0)^2 \quad (\text{S21})$$

where r_{ij}^0 , θ_{ijk}^0 and ϕ_{ijkl}^0 are the equilibrium values of the covalent bond between atoms i and j , the angle between atoms i , j , and k , and the dihedral angle between atoms i , j , k , and l in the molecule, respectively, and K_{ij}^{bond} , K_{ijk}^{angle} , and $K_{ijkl}^{dihedral}$ are the corresponding force constants, all fitted against DFT calculations at the CAM-B3LYP/aug-cc-pVTZ level. The equilibrium covalent bond distances, angles, and dihedral are extracted directly from the fully relaxed molecular geometry. The various force constants are obtained by slightly deforming the optimized geometry along the corresponding degree of freedom and fitting the quadratic energy curve using Eqs. S19-S21. The fits appear in Fig. S11, showing maximal relative deviations between the DFT reference data and the quadratic fits that are lower than 10%. The corresponding values of the fitted parameters appear in Table S5.

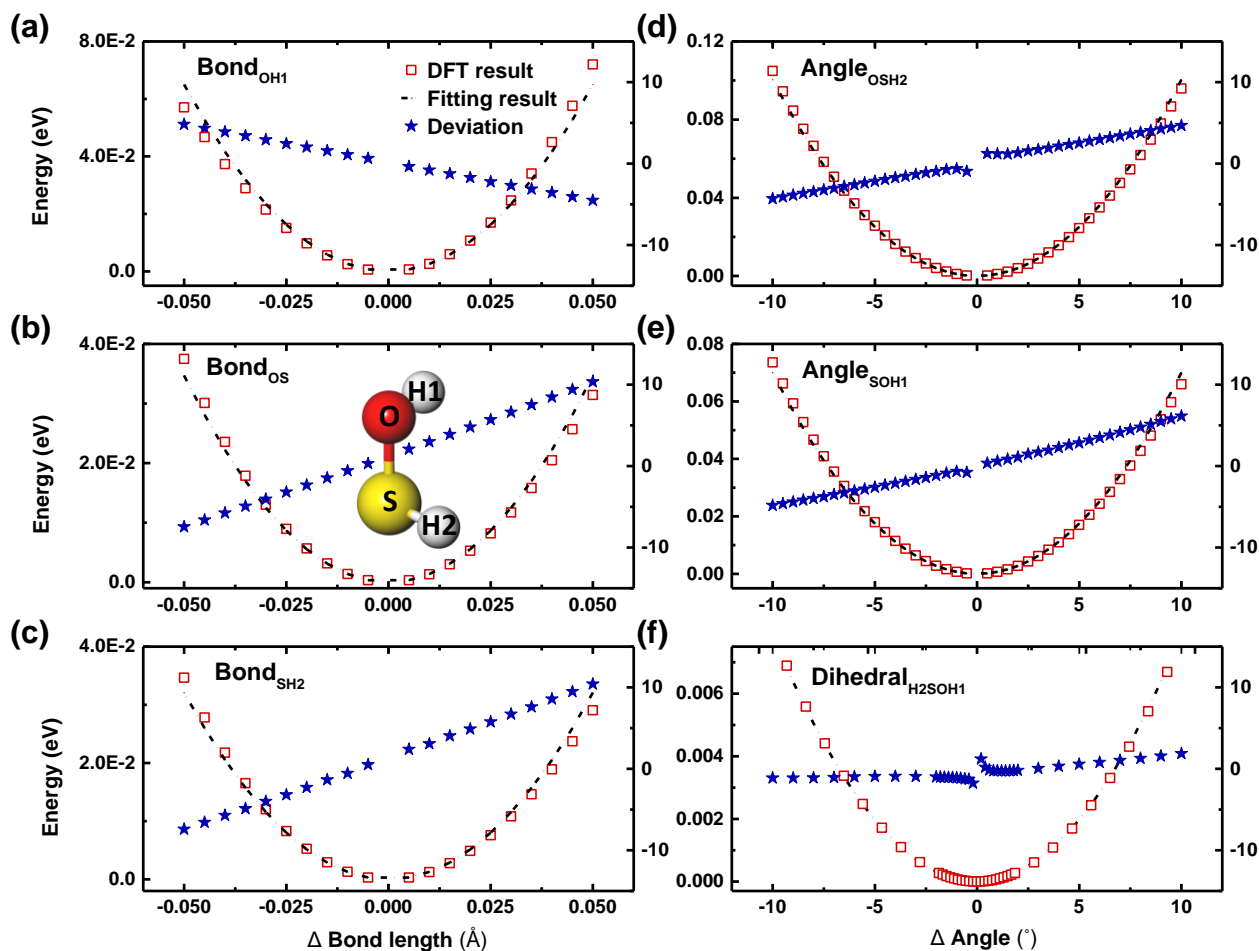


Figure S11: Parabolic fit (dashed-dotted black line) of the HSOH molecular bond (a-c), angle (d-e), and dihedral (f) reference DFT energy curves (open red squares). The relative deviation between the fitted and reference data is presented by the blue stars (right vertical axis).

Table S5: Parameter values for the intra-molecular HSOH (e_2) quadratic interaction terms of Eqs. S19-S21, where the right-hand convention is used for the definition of dihedral angle. Note that in LAMMPS the $\frac{1}{2}$ factor appearing in Eqs. S19-S21 is absorbed in the force constants, such that the values reported herein are twice as large as those fed to the code.

	Bond_{OH1}	Bond_{OS}	Bond_{SH2}
K_{bond} (kcal/mol per \AA^2)	1200	640	592
r_0 (\AA)	0.962	1.669	1.348
	Angle_{OSH2}	Angle_{SOH1}	
K_{angle} (kcal/mol per rad^2)	152	106	
δ_0 (rad)	1.718	1.887	
	Dihedral_{H2SOH1}		
K_{dihedral} (kcal/mol per rad^2)	10.32		
ϕ_0 (rad)	1.606		

To evaluate the importance of molecular flexibility we present in Fig. S12 the ensemble averaged ($N = 18,000$ molecules) relative deviations of various molecular degrees of freedom with respect to their equilibrium values, throughout the scattering processes studied in Fig. 4b of the main text under a static field strength of 500 kV/cm. In all cases, prior to the scattering event, negligible deviations are observed, in accordance with the fact that the simulations are performed at zero temperature. Upon scattering, part of the molecular center-of-mass kinetic energy is transferred to the internal degrees of freedom, as reflected by the increased relative deviations (see Table S6). As expected, these deviations grow with increasing incident velocity, however even at the highest velocity considered (1,500 m/s) they do not exceed $\sim 4\%$ and (well within the harmonic regime¹³) surface collision does not trigger dihedral angle barrier (~ 0.18 eV) crossing that would otherwise racemize the HSOH ensemble upon scattering.¹⁴ We therefore conclude that molecular flexibility has relatively minor effect on the scattering process.

To further demonstrate this, we compare in Fig. S13 the enantiomeric excess obtained in these simulations for rigid (black squares) and flexible (red circles) molecules. Clearly, the qualitative dependence of the enantiomeric excess on the incident velocity remains unaltered when introducing molecular flexibility. Quantitatively, flexibility somewhat reduces the overall enantiomeric excess, where at the highest velocity considered, a reduction from 32% to 25% is obtained. At lower incident velocities even smaller differences are found.

The above analyses thus justify the use of rigid molecules, adopted in the main text.

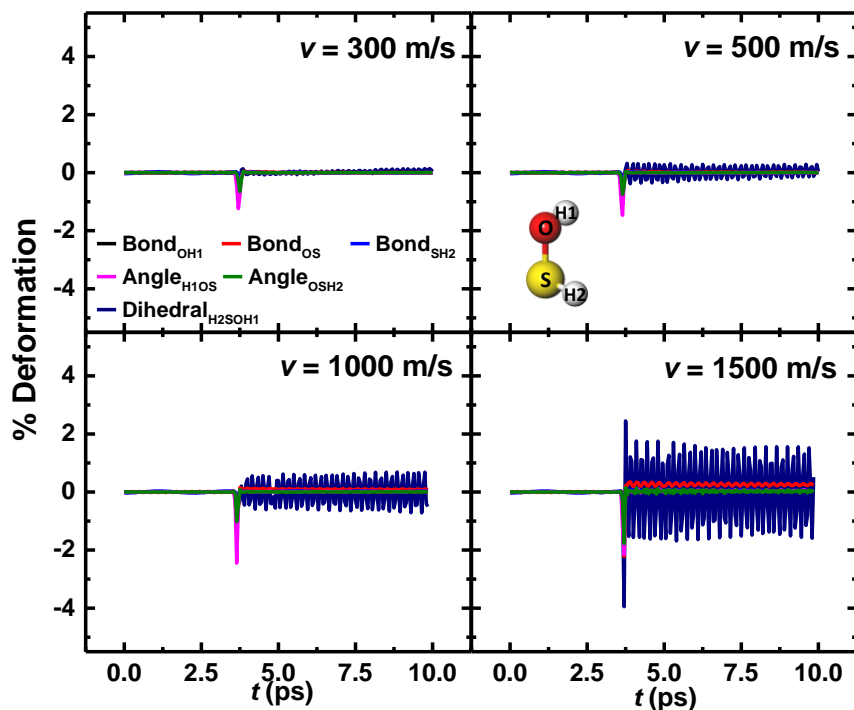


Figure S12: Relative ensemble averaged deformation of the various HSOH molecular degrees of freedom throughout the scattering of flexible molecules under incident velocities of (a) 300, (b) 500, (c) 1,000, and (d) 1,500 m/s (the corresponding initial heights above the surface are set to 15.8, 22.25, 40 and 58.25 Å, respectively) and a static electric field strength of 500 kV/cm. All other parameters are as in Fig. 4b of the main text.

Table S6: Ensemble averaged maximal relative deformation of the various HSOH molecular degrees of freedom throughout the scattering of flexible molecules under incident velocities of 300, 500, 1,000, and 1,500 m/s (the corresponding initial heights above the surface are set to 15.8, 22.25, 40 and 58.25 Å, respectively) and a static electric field strength of 500 kV/cm, with the corresponding standard deviations presented in brackets. All other parameters are as in Fig. 4b of the main text.

Ensemble averaged maximal relative deformation (%)						
Velocity (m/s)	Bond _{OH1}	Bond _{OS}	Bond _{SH2}	Angle _{OSH2}	Angle _{SOH1}	Dihedral _{H2SOH1}
300	-0.17 (0.24)	-0.49 (0.43)	-0.12 (0.31)	-0.65 (0.90)	-1.24 (1.42)	-0.66 (2.33)
500	-0.18 (0.27)	-0.71 (0.45)	-0.17 (0.43)	-0.75 (1.08)	-1.46 (1.68)	-1.12 (3.10)
1000	-0.28 (0.43)	-1.26 (1.00)	-0.29 (0.72)	-1.02 (1.49)	-2.45 (3.18)	-1.38 (5.81)
1500	-0.23 (0.45)	-2.22 (1.13)	-0.30 (0.91)	-1.77 (3.44)	-2.15 (3.30)	-3.95 (8.40)

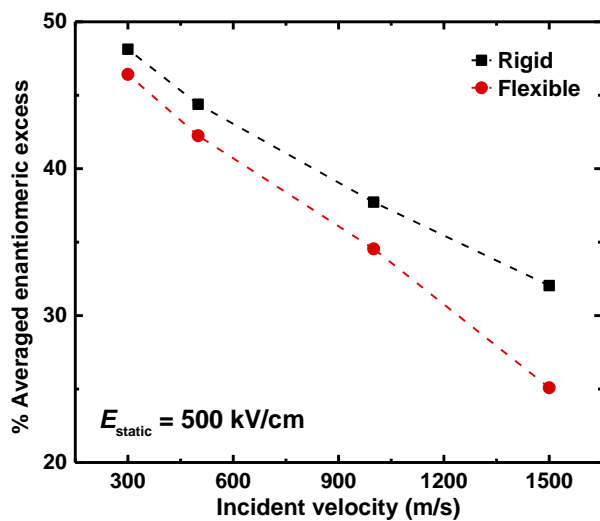


Figure S13: Comparison of the velocity-dependent enantiomeric excesses obtained during the scattering of rigid (black squares) and flexible (red circles) HSOH molecules. All other simulation parameters are as in Fig. S12.

2.7 Thermal effects on HSOH enantio-separation

High pressure pulsed supersonic beam technologies produce molecular ensembles of rotational temperatures down to about 1 K.¹⁵ The relatively high vibrational constants of the molecule assure that at this temperature range it stays in the ground vibrational state (see Table S7 below). To evaluate the effect of rotational excitation on the enantioseparation efficiency, we repeated the calculations (both classical and quantum) at temperatures of $T = 1$ and 2 K, showing that rotational thermal excitation mostly impacts molecular alignment (see Fig. S14), resulting in a reduction of the enantioseparation efficiency from ~48% to ~36% and ~27%, respectively, at an incident velocity of 300 m/s (see Fig. S15). While, indeed we see that enantioseparation is affected by rotational thermal excitation, the obtained separation efficiencies remain quite high and can be further improved by applying stronger alignment pulse intensities.

Table S7: Vibrational and rotational constants of HSOH.¹³

	Vibrational constant (cm^{-1})		Rotational constant (cm^{-1})
Bond _{OH1}	3625.9	I_x	6.7403
Bond _{SO}	760	I_y	0.5098
Bond _{SH2}	2544.4	I_z	0.495
Angle _{OSH2}	1007.7		
Angle _{H1OS}	1174		
Dihedral _{H2SOH1}	443		

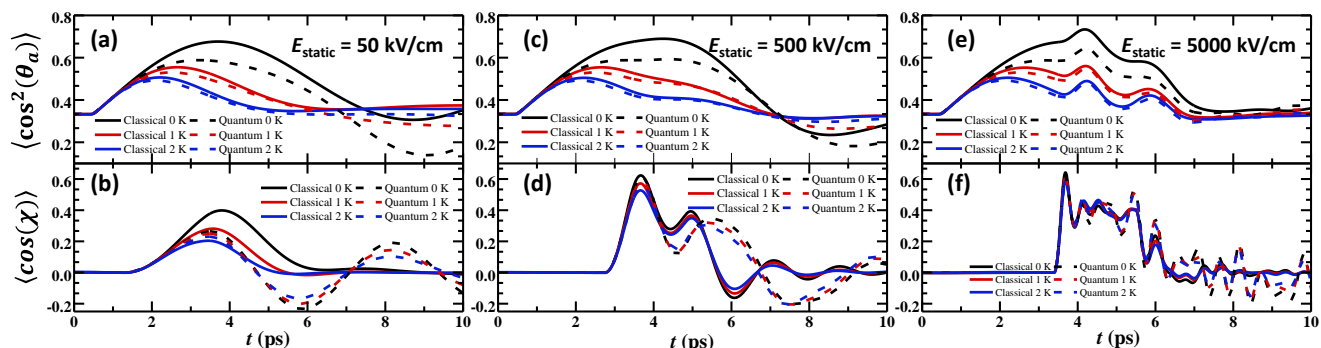


Figure S14: Comparison between classical (full lines) and quantum mechanical (dashed lines) alignment (upper panels) and orientation (lower panels) factor dynamics of an initially randomly oriented ensemble of $N = 18,000$ rigid HSOH molecules at the temperature of $T = 0, 1,$ and 2 K (black, red, and blue lines) under static field strengths of 50 (left panels), 500 (middle panels), and $5,000$ (right panels) kV/cm, applied at time delays of $0.8,$ $2.25,$ and 2.9 ps from the peak alignment pulse intensity, respectively. The alignment pulse parameters are as in Fig. S6.

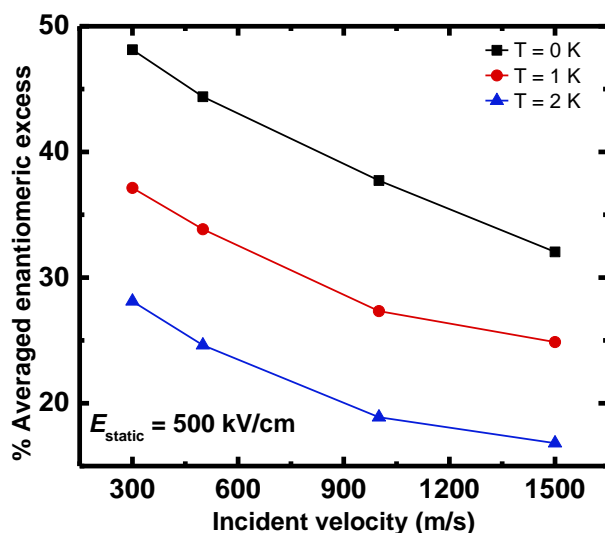


Figure S15: Effect of temperature on the velocity dependence of the enantiomeric excesses of an initially randomly oriented ensemble of $N = 18,000$ rigid HSOH molecules under a static field strength of 500 kV/cm, applied at time delays of 2.25 ps from the peak alignment pulse intensity via classical mechanical simulation. All other simulation parameters are as in Fig. S6b.

2.8 HSOH enantio-separation under parallel alignment conditions

In the main text, we presented an opto-mechanical chiral resolution scheme based on a sequence of molecular alignment, dipole orientation, and dissipative surface scattering. It was stated that aligning the main axis of the HSOH molecules perpendicular to the scattering surface provides the highest enantio-separation efficiency. To support this statement, we repeated some of our rigid molecular scattering simulations, where the alignment pulse drives the SO bond to lie parallel to the surface and perpendicular to the direction of the static electric field (see inset of Fig. S16b). Naturally, changing the molecular orientation upon surface impact requires reoptimizing some of the scattering parameters to obtain maximal enantio-separation efficiency. Specifically, when keeping the alignment pulse parameters the same as in the vertical alignment scattering process, and considering static electric fields of 50, 500, and 5,000 kV/cm, one needs to shorten the time delay between the alignment pulse peak and the application of the static electric field to 0.6, 0.8, and 1.2 ps, respectively. Fig. S16a presents the corresponding scattering angular distributions of the two enantiomers at an incident velocity of 1,000 m/s. Similar to the case of vertical alignment scattering, clear spatial enantio-separation is obtained, where a static field strength of 500 kV/cm provides higher enantio-separation than the field of 50 kV/cm. Nevertheless, the overall enantio-separation efficiency is about twice as low in the parallel alignment scattering as in the vertical case. Furthermore, at lower incident velocities, the application of a static field strength of 500 kV/cm yields lower enantiomeric excess than the case of 5,000 kV/cm (see Fig. S16b).

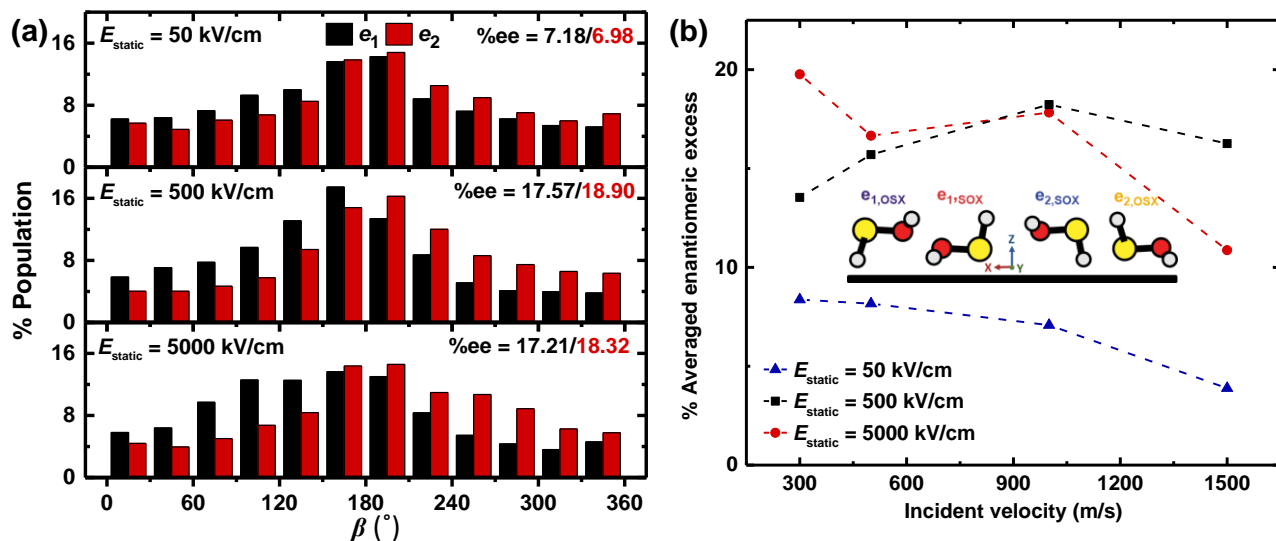


Figure S16: Effect of field strength and incident velocity on enantio-selectivity for an initially uniformly distributed randomly oriented ensemble of $N = 18,000$ HSOH rigid molecules experiencing parallel alignment optical manipulations. (a) Angular distributions of the two enantiomers (black and red columns) with an initial vertical collision velocity of 1,000 m/s for static field strengths of 50, 500, and 5,000 kV/cm at time delays of 0.6, 0.8, and 1.2 ps, respectively, from the maximal intensity of the Gaussian alignment pulse ($\sigma = 0.1$ ps, $E_0 = 84.85$ MV/cm, and $t_0 = 0.5$ ps) centered at the beginning of the simulation. The corresponding initial heights above the surface are 38, 27 and 24 Å, respectively. (b) Velocity-dependent enantiomeric excesses at static field strengths of 50, 500, and 5,000 kV/cm. In these cases, scattering from a surface of kinetic friction coefficient of $\mu_k = 0.3$, occurs at $t = \sim 3.6, \sim 2.5,$ and ~ 2.1 ps, respectively.

We attribute the lower enantio-separation efficiency obtained for the surface parallel alignment case to the fact that at this configuration the molecular ensemble attains a higher rotational energy upon impact (see Fig. S17a) and hence loses its optimal average orientation faster within the surface interaction range (see Fig. S17b). These results therefore support our statement that for the HSOH molecule, vertical alignment scattering provides higher enantio-separation efficiency.

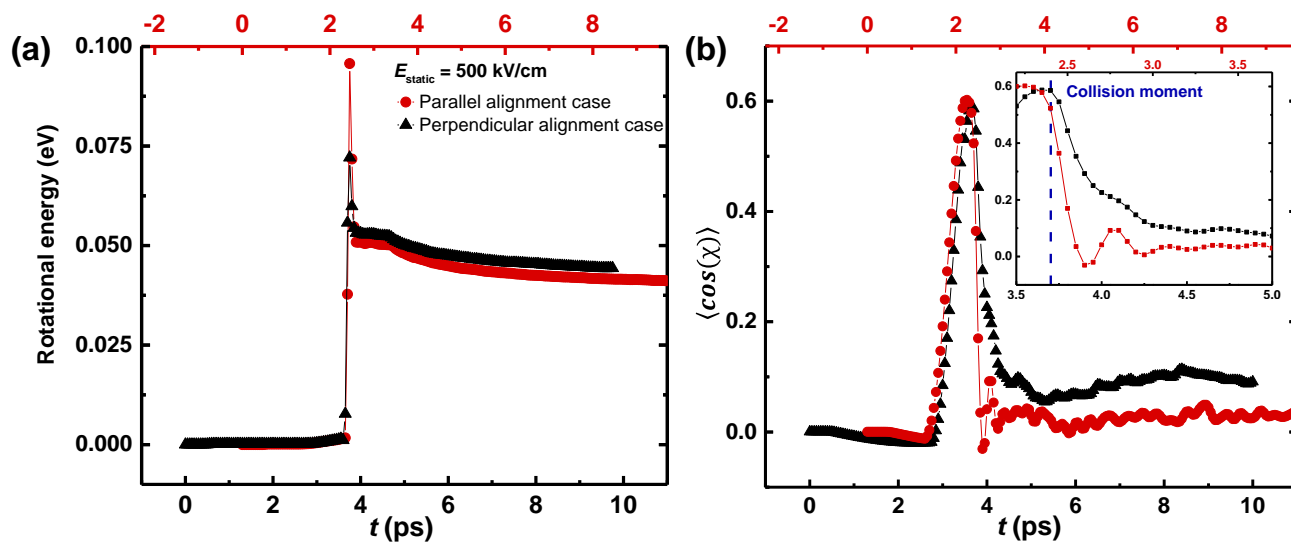


Figure S17: Comparison of the time evolution of the ensemble averaged (a) rotational energy and (b) dipole orientation factor $\langle \cos(\chi) \rangle$ of an ensemble of 18,000 initially uniformly distributed randomly oriented rigid HSOH molecules, optically aligned perpendicular (black) or parallel (red) to a surface prior to scattering. The static electric field strength is 500 kV/cm. All other simulation parameters are the same as those used to obtain maximal enantio-selectivity with an initial incident velocity of $v = 1,000$ m/s for the perpendicular (see Fig. S6) and parallel (see Fig. S16) alignments.

2.9 HSOH enantiomeric scattering under a permanent uniform electric field

Current experimental capabilities are still unable to provide high optical spatial precision as that required by the proposed approach. Hence, using currently available technology a large portion of the molecular ensemble will experience the laser pulse too early during its vertical trajectory towards the surface, and will not be appropriately aligned. Such molecules can be considered to experience only the static electric field when approaching the vicinity of the scattering surface. As a lower bound for the enantiomeric separation efficiency, one can therefore consider the efficiency given by the case of molecular scattering in the presence of a static electric field alone. The second panel from the top in Fig. 3c of the main text demonstrates that in this case the enantiomeric excess is roughly 11% - still quite significant. Further improvement can be obtained by continuously applying the static electric field also during the pulse application, thus effectively eliminating the delay time between them. The results of these calculations appear in Fig. S18 below demonstrating enantiomeric excesses as high as ~20% for HSOH molecules.

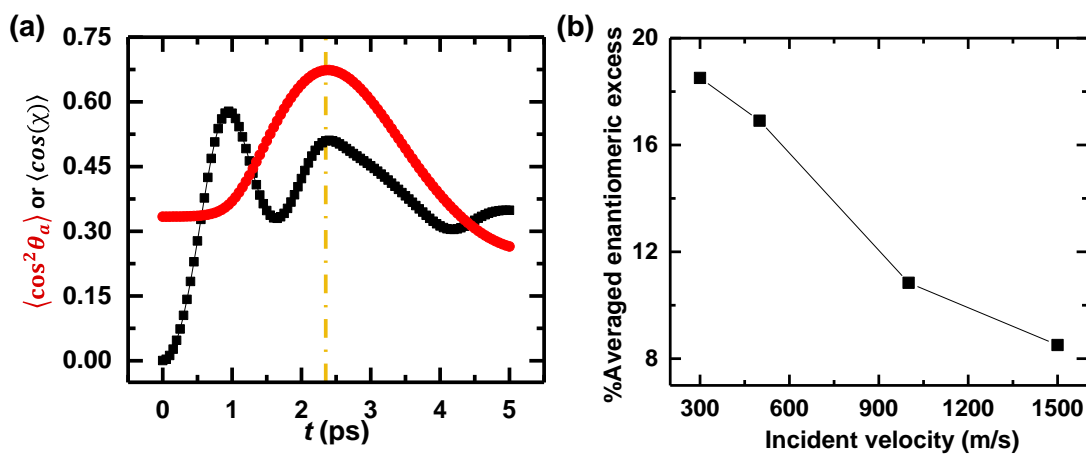


Figure S18: Enantioselectivity of the proposed frictional enantio-separation approach with the simultaneous application of a Y-directional orienting static electric field of 500 kV/cm and an alignment laser pulse ($\sigma = 0.5$ ps, $E_0 = 50 \frac{MV}{cm}$, $t_0 = 1.0$ ps) polarized in the Z direction. (a) Time evolution of the alignment $\langle \cos^2(\theta_a) \rangle(t)$ and orientation $\langle \cos(\chi) \rangle(t)$ factors for an ensemble of $N = 18,000$ HSOH rigid molecules, the initial orientations of which are randomly chosen from a uniform distribution. (b) Velocity-dependent enantiomeric excesses, where the corresponding initial heights above the surface are 12, 15.75, 27 and 38.75 Å for the velocity of 300, 500, 1,000 and 1,500 m/s, respectively. In these cases, scattering from a surface of kinetic friction coefficient of $\mu_k = 0.3$ occurs at $t = \sim 2.35$ ps (corresponding to the yellow dashed line in panel a).

Section 3. Separation of propylene oxide (C₃H₆O) enantiomers

To demonstrate the broad applicability of the proposed frictional enantio-separation approach, we performed additional simulations replacing the HSOH molecule with propylene oxide - the first chiral molecule discovered in interstellar space, which possesses considerably higher racemization barriers.^{16,17} Table S8 presents the relevant properties of propylene oxide (*S* enantiomer) in the *C* and *M* reference frames (see section 1.1 above), including eigenvalues of the inertia tensor, permanent dipole moment, and independent polarizability tensor elements. Table S9 provides the homogeneous 12-6 interaction parameters for the different atoms of this molecule (see section 1.2 above) as given in the OPLS-AA force-field.¹⁸ All calculations of the propylene oxide molecules are performed with a rigid molecular model and a fixed propagation time step of 0.01 fs that provides adequate energy conservation for frictionless dynamics.

Table S8: Eigenvalues of the inertia tensor, components of the permanent dipole moment, and independent polarizability tensor elements calculated for the (*S*)-C₃H₆O enantiomers. All values are presented in both the *C* and *M* reference frames. For the complementary enantiomer, the values of $P_{0,x}$, α_{xy} and α_{xz} have opposite signs.

Molecule	In the body frame of the principal inertia axes of COC				In the body frame of the principal inertia axes of COM			
	Moments of inertia (a.u.)	Dipole moment components (Debye)	Polarizability tensor components (a.u.)		Moments of inertia (a.u.)	Dipole moment components (Debye)	Polarizability tensor components (a.u.)	
C ₃ H ₆ O (<i>es</i>)	$I_x = 65.6$	$P_{0,x} = 0.878$	$\alpha_{xx} = 45.825$	$\alpha_{xy} = -2.289$	$I_x = 178460$	$P_{0,x} = -0.966$	$\alpha_{xx} = 45.630$	$\alpha_{xy} = -2.561$
	$I_y = 170.1$	$P_{0,y} = 1.704$	$\alpha_{yy} = 37.895$	$\alpha_{xz} = 0.732$	$I_y = 488054$	$P_{0,y} = -1.733$	$\alpha_{yy} = 37.963$	$\alpha_{xz} = -0.852$
	$I_z = 183.8$	$P_{0,z} = 0.705$	$\alpha_{zz} = 37.744$	$\alpha_{yz} = -0.639$	$I_x = 547305$	$P_{0,z} = 0.488$	$\alpha_{zz} = 37.868$	$\alpha_{yz} = 0.648$

Table S9: Summary of LJ 12 – 6 homogeneous parameters for propylene oxide.

Molecule	Atom	η (Å)	ϵ (kcal/mol)
<i>(S)</i> -C ₃ H ₆ O	O	2.9	0.14006
	C1	3.5	0.06597
	H1	2.5	0.02940
	H2	2.5	0.02940
	H3	2.5	0.02940
	C2	3.5	0.06597
	H4	2.5	0.03011
	C3	3.5	0.06597
	H5	2.5	0.03011
	H6	2.5	0.03011

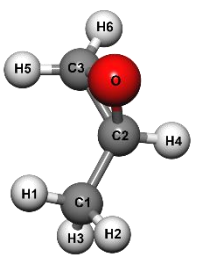


Fig. S19a shows the azimuthal scattering angle distributions of the two enantiomers, given an initial center of mass velocity of 1,000 m/s, when the Gaussian laser pulse ($\sigma = 0.1$ ps, $E_0 = 161 \frac{\text{MV}}{\text{cm}}$, $t_0 = 0.5$ ps) is polarized along the z (top panel) and x (bottom panel) directions followed by (time delay of 2.8 ps from the maximal pulse intensity) a static electric field of 15,000 kV/cm along the y -direction. Such static fields are currently achievable using tip-shaped electrodes.^{19–21} Similar to the case of HSOH, perpendicular alignment of the propylene oxide molecules generally leads to more efficient enantiomeric separation compared to parallel alignment conditions with a maximal value obtained at 15,000 or 20,000 kV/cm, respectively (see Fig. 19b). Such high field intensities are required since the moment of inertia of propylene oxide is significantly greater than that of HSOH, whereas their dipole moments are comparable. Figure S19c presents the effect of initial incident velocity on the frictional enantioselectivity of $\text{C}_3\text{H}_6\text{O}$ enantiomers under an electric field intensity of 15,000 kV/cm showing maximal efficiency (~20 % under perpendicular alignment condition) at 1,000 m/s. The predicted efficiency is comparable to that previously reported using a different optical enantio-separation scheme of the same molecule.²²

These results exemplify the fact that the efficiency of the proposed scheme depends on the angle between the permanent molecular dipole moment and the axis of maximal polarizability. In the case of the HSOH molecule, where the two are nearly orthogonal, the maximal enantio-separation efficiency is higher than for the propylene oxide molecule that possesses an angle of $\sim 77^\circ$ between the permanent molecular dipole moment and the axis of maximal polarizability. This results from a reduction in the degree of molecular alignment during the process of dipole orientation (see Fig. S20). Nonetheless, the efficiency remains high also in the latter case, demonstrating that our approach is applicable to a wide family of polar molecules.

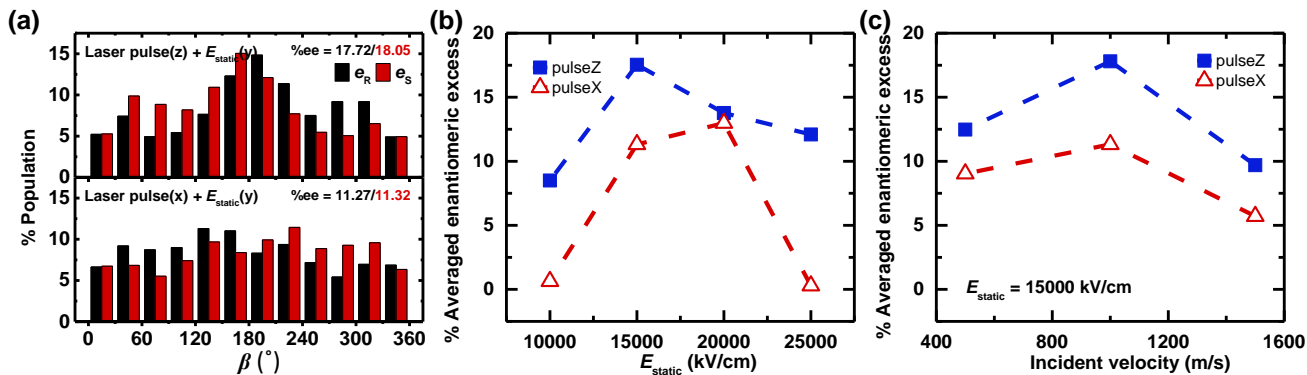


Figure S19: Enantioselectivity of propylene oxide enantiomers. (a) Azimuthal scattering distributions for an ensemble of $N = 18,000$ C_3H_6O rigid molecules, the initial orientations of which are randomly chosen from a uniform distribution, in the perpendicular and parallel alignment conditions with an initial velocity of 1,000 m/s, where the Y-directional orienting static field of 15,000 kV/cm is applied with a time delay of 2.8 ps from the maximal pulse intensity of the alignment Gaussian pulse ($\sigma = 0.1$ ps, $E_0 = 161 \frac{MV}{cm}$, $t_0 = 0.5$ ps). (b) Enantiomeric excesses at static electric field strengths of 10,000, 15,000, 20,000 and 25,000 kV/cm, for both alignment conditions with an initial incident velocity of 1,000 m/s. (c) Velocity-dependent enantiomeric excesses at the static field strength of 15,000 kV/cm, for both alignment conditions. In these cases, scattering from a surface of kinetic friction coefficient of $\mu_k = 0.3$ occurs at $t = \sim 4$ ps, and the corresponding initial heights above the surface are 16, 39 and 57.5 Å for the velocity of 300, 1,000 and 1,500 m/s, respectively.

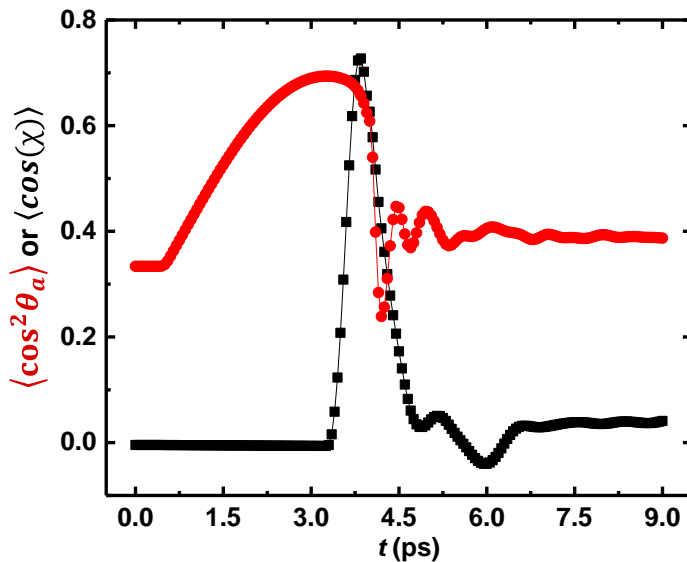


Figure S20: Time evolution of the alignment $\langle \cos^2(\theta_a) \rangle(t)$ and orientation $\langle \cos(\chi) \rangle(t)$ factors for an ensemble of $N = 18,000$ C_3H_6O rigid molecules of initial molecular orientations that are randomly chosen from a uniform distribution and given an initial center of mass velocity of 1,000 m/s. Perpendicular Gaussian pulse ($\sigma = 0.1$ ps, $E_0 = 161 \frac{MV}{cm}$, $t_0 = 0.5$ ps) alignment conditions are considered with a y-directional orienting static field of 15,000 kV/cm applied with a time delay of 2.8 ps from the maximal pulse intensity. Under these conditions, scattering occurs from the frictional surface of kinetic friction coefficient $\mu_k = 0.3$ at $t = \sim 4$ ps.

References

- (1) Sussman, B. J. Five Ways to the Nonresonant Dynamic Stark Effect. *Am. J. Phys.* **2011**, *79* (5), 477–484. <https://doi.org/10.1119/1.3553018>.
- (2) Gershnel, E.; Averbukh, I. S. Orienting Asymmetric Molecules by Laser Fields with Twisted Polarization. *Phys. Rev. Lett.* **2018**, *120* (8), 83204. <https://doi.org/10.1103/PhysRevLett.120.083204>.
- (3) Koch, C. P.; Lemeshko, M.; Sugny, D. Quantum Control of Molecular Rotation. *Rev. Mod. Phys.* **2019**, *91* (3), 035005. <https://doi.org/10.1103/RevModPhys.91.035005>.
- (4) Frisch, M. J.; Trucks, G. W.; Schlegel, H. B.; Scuseria, G. E.; Robb, M. A.; Cheeseman, J. R.; Scalmani, G.; Barone, V.; Petersson, G. A.; Nakatsuji, H. et al. Gaussian 16. Gaussian, Inc. Wallingford, CT 2016.
- (5) Israelachvili, J. N. *Intermolecular and Surface Forces*; Academic press, 2011.
- (6) Hummer, G.; Rasaiah, J. C.; Noworyta, J. P. Water Conduction through the Hydrophobic Channel of a Carbon Nanotube. *Nature* **2001**, *414* (6860), 188–190. <https://doi.org/10.1038/35102535>.
- (7) Jorgensen, W. L.; Maxwell, D. S.; Tirado-Rives, J. Development and Testing of the OPLS All-Atom Force Field on Conformational Energetics and Properties of Organic Liquids. *J. Am. Chem. Soc.* **1996**, *118* (45), 11225–11236. <https://doi.org/10.1021/ja9621760>.
- (8) Yanai, T.; Tew, D. P.; Handy, N. C. A New Hybrid Exchange–Correlation Functional Using the Coulomb-Attenuating Method (CAM-B3LYP). *Chem. Phys. Lett.* **2004**, *393* (1–3), 51–57. <https://doi.org/10.1016/j.cplett.2004.06.011>.
- (9) Plimpton, S. Fast Parallel Algorithms for Short-Range Molecular Dynamics. *J. Comput. Phys.* **1995**, *117* (1), 1–19. <https://doi.org/10.1006/jcph.1995.1039>.
- (10) Jankunas, J.; Osterwalder, A. Cold and Controlled Molecular Beams: Production and Applications. *Annu. Rev. Phys. Chem.* **2015**, *66* (1), 241–262. <https://doi.org/10.1146/annurev-physchem-040214-121307>.
- (11) Tutunnikov, I.; Floß, J.; Gershnel, E.; Brumer, P.; Averbukh, I. S. Laser-Induced Persistent Orientation of Chiral Molecules. *Phys. Rev. A* **2019**, *100* (4), 043406. <https://doi.org/10.1103/PhysRevA.100.043406>.
- (12) Tutunnikov, I.; Xu, L.; Field, R. W.; Nelson, K. A.; Prior, Y.; Averbukh, I. S. Enantioselective Orientation of Chiral Molecules Induced by Terahertz Pulses with Twisted Polarization. *Phys. Rev. Res.* **2021**, *3* (1), 013249. <https://doi.org/10.1103/PhysRevResearch.3.013249>.
- (13) Yurchenko, S. N.; Yachmenev, A.; Thiel, W.; Baum, O.; Giesen, T. F.; Melnikov, V. V.; Jensen, P. An Ab Initio Calculation of the Vibrational Energies and Transition Moments of HSOH. *J. Mol. Spectrosc.* **2009**, *257* (1), 57–65. <https://doi.org/10.1016/j.jms.2009.06.010>.

- (14) Yachmenev, A.; Yurchenko, S. N. Detecting Chirality in Molecules by Linearly Polarized Laser Fields. *Phys. Rev. Lett.* **2016**, *117* (3), 033001. <https://doi.org/10.1103/PhysRevLett.117.033001>.
- (15) Kumarappan, V.; Bisgaard, C. Z.; Viftrup, S. S.; Holmegaard, L.; Stapelfeldt, H. Role of Rotational Temperature in Adiabatic Molecular Alignment. *J. Chem. Phys.* **2006**, *125* (19), 194309. <https://doi.org/10.1063/1.2388273>.
- (16) McGuire, B. A.; Carroll, P. B.; Loomis, R. A.; Finneran, I. A.; Jewell, P. R.; Remijan, A. J.; Blake, G. A. Discovery of the Interstellar Chiral Molecule Propylene Oxide (CH₃CHCH₂O). *Science* **2016**, *352* (6292), 1449–1452. <https://doi.org/10.1126/science.aae0328>.
- (17) Xie, F.; Seifert, N. A.; Hazrah, A. S.; Jäger, W.; Xu, Y. Conformational Landscape, Chirality Recognition and Chiral Analyses: Rotational Spectroscopy of Tetrahydro-2-Furoic Acid···Propylene Oxide Conformers. *ChemPhysChem* **2021**, *22* (5), 455–460. <https://doi.org/10.1002/cphc.202000995>.
- (18) Kiss, B.; Szöri, M.; Jedlovszky, P. Adsorption of Propylene Oxide on Amorphous Ice under Interstellar Conditions. A Grand Canonical Monte Carlo Simulation Study. *J. Phys. Chem. C* **2020**, *124* (30), 16402–16414. <https://doi.org/10.1021/acs.jpcc.0c03722>.
- (19) Scovell, D. L.; Pinkerton, T. D.; Medvedev, V. K.; Stuve, E. M. Phase Transitions in Vapor-Deposited Water under the Influence of High Surface Electric Fields. *Surf. Sci.* **2000**, *457* (3), 365–376. [https://doi.org/10.1016/S0039-6028\(00\)00383-6](https://doi.org/10.1016/S0039-6028(00)00383-6).
- (20) Hsu, P. J.; Kubetzka, A.; Finco, A.; Romming, N.; Von Bergmann, K.; Wiesendanger, R. Electric-Field-Driven Switching of Individual Magnetic Skyrmions. *Nat. Nanotechnol.* **2017**, *12* (2), 123–126. <https://doi.org/10.1038/nnano.2016.234>.
- (21) English, N. J. Electric-Field-Promoted Photo-Electrochemical Production of Hydrogen from Water Splitting. *J. Mol. Liq.* **2021**, *342*, 116949. <https://doi.org/10.1016/j.molliq.2021.116949>.
- (22) Yachmenev, A.; Onvlee, J.; Zak, E.; Owens, A.; Küpper, J. Field-Induced Diastereomers for Chiral Separation. *Phys. Rev. Lett.* **2019**, *123* (24), 243202. <https://doi.org/10.1103/PhysRevLett.123.243202>.